PAPER

Crack sensor based on patch antenna fed by capacitive microstrip lines

IOP Publishing Smart Materials and Structures
Smart Mater. Struct. **28** (2019) 085012 (13pp) https://doi.org/10.1088/1361-665X/ab2834

Crack sensor based on patch antenna fed by capacitive microstrip lines

Songtao Xue[1,2], Kangqian Xu[1], Liyu Xie[1] and Guochun Wan[3]

[1] Department of Disaster Mitigation for Structures, Tongji University, Shanghai, People's Republic of China
[2] Department of Architecture, Tohoku Institute of Technology, Sendai, Japan
[3] Department of Electronic Science and Technology, Tongji University, Shanghai, People's Republic of China

E-mail: liyuxie@tongji.edu.cn

Received 24 February 2019, revised 14 May 2019
Accepted for publication 10 June 2019
Published 1 July 2019

Abstract

When sensors based on a single patch antenna are used to monitor crack width, the issues of incomplete strain transfer ratio, insufficient bonding strength, and randomness of crack propagation will inevitably compromise sensor sensitivity and make the calibration uncontrollable. To circumvent these difficulties, this study presents a novel crack-measuring sensor based on a rectangular patch antenna fed by a pair of microstrip lines, which form a parallel plate capacitor as a crack-sensing unit. The sensing mechanism was analyzed using the transmission-line model. Then two crack sensor prototypes were designed and the dimensions were optimized. A crack opening simulator was customized to test the sensors by using different width resolutions. The experiment results validated that the resonant frequency shifts are linearly proportional to the applied crack width; moreover, the crack sensor proved capable of detecting crack widths as small as one-hundredth of a millimeter in an object.

Keywords: passive wireless sensor, patch antenna, crack monitoring, capacitive microstrip line

(Some figures may appear in colour only in the online journal)

1. Introduction

Over time, structural service loads and environmental effects will cause a gradual degradation of structural performance; thus, technologies dedicated to structural health monitoring have been extensively developed over the last few decades [1].

Since cracks can directly indicate the degree of structural damage, crack monitoring is essential to structural health monitoring. For reinforced concrete structures, lots of factors can induce cracks, such as excessive loads, differential settlement, temperature variations, and so on. Cracks will accelerate the carbonation of concrete and the corrosion of their reinforcing steel bars, make a building appear old and unsightly, adversely decrease the carrying capacity of structures [2]. For steel structures, cracks are usually induced by fatigue under cycling loads [3]. Most importantly, a structure can fail and rupture suddenly when the dimensions of its cracks exceed the critical value [4]. The crack width can be assessed by visual inspection with the help of a magnifying lens or by ultrasonic testing [5]. However, manual inspection should be conducted periodically, which is time- and labor-consuming. In structural health monitoring, crack sensing technology is extensively used, such as the fiber optical crack sensor [6]. The performance of these traditional crack sensors is reliable. However, cables are needed to supply both the power supply and data transmission for these sensors, which makes installation and deployment of crack sensors difficult and costly. Furthermore, wired crack sensors cannot acquire data because of power failure or cable malfunction during extreme disasters when they are most needed.

To get rid of sensing system lines and cables entirely, passive wireless sensors were developed and applied. The antennas based on oscillating circuits with the help of inductors were developed for strain sensing [7]. Later, sensors utilizing low-profile antennas, such as patch antennas and dipole antennas, received more attention due to their smaller size [8]. The deformation on structure surfaces caused by strain or cracks could then be transferred to the antennas attached to the structures.

The passive antenna sensors for deformation monitoring can be divided into two categories based on the sensing mechanism [9]. The first category is the radio-frequency identification (RFID)-enabled antenna sensors. In this case, the antenna sensors have the dual function of deformation sensing and data transmission. The dimension change of the radiation patch induced by structural deformation will affect the resonant frequency of the patch antenna. For instance, Daliri *et al* [10] fabricated a chipless sensor based on a circular patch antenna. Yi *et al* [11, 12] developed a smart-skin chipped sensor based on the folded patch antenna using radio frequency identification technology [13, 14]. Moreover, other congeneric antenna sensors have been developed for this purpose [15, 16]. The second category of passive antenna sensors is the impedance load-based sensor. In this case, the structural deformation will result in the impedance change of the antenna load, and subsequently alter the electromagnetic parameters of the antenna. Thus, the impedance of the load is the sensing element used to measure the desired physical parameters. Thai *et al* [17, 18] designed a highly sensitive sensor based on a patch antenna loaded with an open loop for strain sensing. The overlapped length of the capacitance area is altered when the structural deformation is transferred to the top surface of the patch, leading to the impedance change of the antenna load and a shift in the resonant frequency of the patch antenna.

Therefore, crack sensors can be fabricated based on the sensing mechanism wherein the electromagnetic properties of the antenna vary with its deformation or load. However, some unsolved problems were confronted when these crack sensors of monolithic patch antennas were actually designed and tested. Since the deformation sensing unit is on the top surface of the antenna, the deformation induced by a crack could not be fully transferred to the top surface of the antenna due to the shear lag effect [19] caused by the non-negligible thickness of the substrate and the plastic flow of adhesive materials. As a result, the strain transfer ratio between the top antenna and the bonded surface of the structures must be calibrated carefully, and it depends on the type of superglue and the surface material; an accurate strain transfer ratio also depends on the evenness and thickness of the superglue during the manual bonding operation. An unsettled strain transfer ratio can hold back the industrial production and commercialization of crack sensors using monolithic patch antennas as their sensing units.

Another issue is associated with the stress concentration occurring at the tip of the crack during the crack propagation. An antenna can be torn apart by the stress concentration, which subsequently affects the induced electromagnetic field on the radiation patch and shift the resonant frequency of antennas [20]. However, the formation of cracks on radiation patches is random even under the same conditions, which means the crack sensor will perform differently with different crack paths. The third problem is caused by the bonding strength of the superglue. The crack sensor based on one-piece patch antennas is usually glued onto the surface of the structure by adhesive materials. When the strain is at a high level, the bonding between the crack sensors and structures fails due to the insufficient bonding strength. The bonding strength can be improved by bolted connections and welding, but the electromagnetic property of the antenna will be significantly modified because the substrate of the antenna needs to have a punched hole and the copper cladding of the ground plane is prone to melt at the soldering point, respectively.

When monolithic patch antennas are adopted for sensing, these problems can be especially stubborn. To circumvent these difficulties, Caizzone *et al* [21] and Caizzone and Digiampaolo [22] proposed crack sensors, which used two mutual-coupling planar-inverted-inverted-F antennas. Each antenna was placed on one side of the crack. The coupled antennas' phase changed with the relative displacement between the two antennas as the crack propagated. So, the crack width can be measured if the relationship between the relative displacement and phase of the coupled antennas was established. Nevertheless, the interrogation distance between the coupled antennas and reader affected the measured phase, which confirms that the reader position must be fixed through the whole monitoring process. This made the proposed crack sensors in [21, 22] inflexible and, therefore, unsuitable for real applications. Despite the quantifiable issue of using antennas as crack sensors, the idea of coupled antennas shed new light on the possibility of developing a crack sensor using detachable or separable antennas instead of using one-piece patch antennas.

To avoid the issues of the incomplete strain transfer ratio, randomness of crack propagation and insufficient bonding strength, the authors developed a novel crack sensor based on a rectangular patch antenna fed by a pair of capacitive microstrip lines with a cantilevered structure, forming a parallel plate capacitive cell between microstrip lines. The monolithic patch antenna lies on one side of a crack and the cantilevered part of the crack sensor lies on the other side. The capacitive cell, as the load of the patch antenna, serves as the crack sensing unit, and the measured resonant frequency of proposed sensors detect the crack width with a reliability that is not affected by interrogation range, transmission losses, or other interferences. This paper is organized as follows: section 2 introduces the concept of crack sensors with capacitive microstrip lines and simplifies the sensor using the transmission-line model. In this section, two prototypes of the cantilevered microstrip lines are described and the dimension of two prototype sensors are optimized by modeling. Section 3 presents the modeling and simulation of crack sensors. The appropriate sensing parameters are determined by the mode analysis of two prototypes and the return loss curves for each sensor are obtained by frequency sweeping. Section 4 describes the fabrication of sensors and the instrumentation setup of experiments. The sensing performance of each crack sensor is depicted. Section 5 draws the conclusions and summarizes the potential of this research.

2. Crack sensor with capacitive microstrip lines

A novel crack sensor using a conventional rectangular patch antenna is proposed by altering its microstrip line by pairing the bottom microstrip line with the upper microstrip line to form a capacitor between them, which make up the load of the

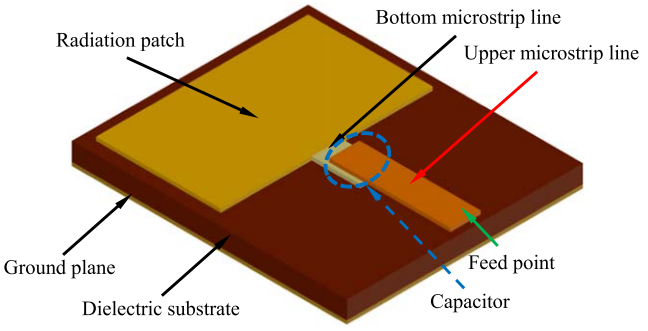

(a) Concept of crack sensor with capacitive microstrip lines

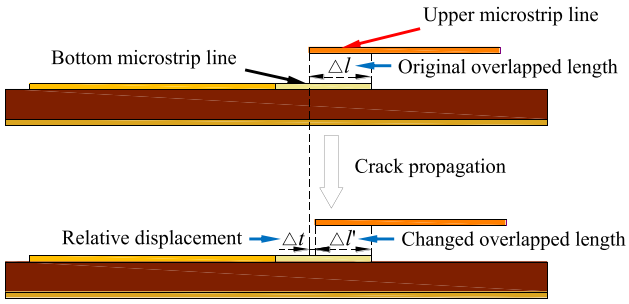

(b) Relative displacement of two components

Figure 1. A novel crack sensor with capacitive microstrip lines.

patch antenna. The bottom microstrip line is overlapped by the upper microstrip line forming a parallel plate capacitor. The constant gap between them can be filled with air or isotropic dielectric materials. The overlapped length of the bottom microstrip line and upper microstrip line is pertinent to the impedance of the patch antenna load, consequently influencing the dominant resonant frequencies of the crack sensor. As a result, the parallel capacitor can function as the sensing unit for the crack width. The cantilever structure of the upper microstrip line avoids the problems we encountered before, such as the sensor-structure connecting issues and compromised strain transfer efficiency due to shear lag effect of the non-negligible thickness of the patch and adhesive glue.

The novel crack sensor has two components illustrated in figure 1(a). One part includes a one-piece radiation patch, ground plane, substrate, and bottom microstrip line, and the other part includes the upper microstrip line. No attachment exists between the pair of microstrip lines, which can relatively move without constraint, as shown in figure 1(b). The radiation patch is fed at the edge of the upper microstrip line.

2.1. Equivalent-circuit model of proposed crack sensor

A conventional rectangular patch antenna is modeled by a parallel twin wire transmission line shown in figure 2. Assuming the length of transmission line is l, the characteristic impedance of the transmission line is Z_0, and the impedance of load is Z_L, the input impedance of the patch antenna can be calculated as [23]

$$Z_{\text{in}} = Z_0 \frac{Z_L + Z_0 \tan \beta l}{Z_0 + Z_L \tan \beta l}, \tag{1}$$

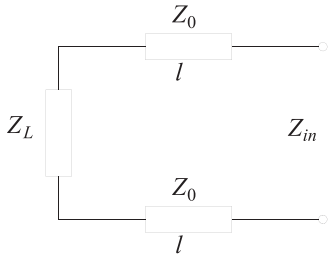

Figure 2. The model of transmission line for a patch antenna.

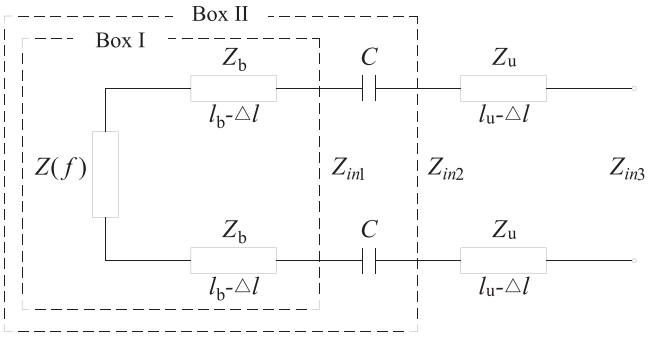

Figure 3. The equivalent circuit of crack sensor.

where the parameter β can be estimated as

$$\beta = \frac{2\pi}{\lambda_g}\sqrt{\varepsilon_e} = \frac{2\pi f}{c}\sqrt{\varepsilon_e}, \tag{2}$$

where λ_g is the wavelength of the electromagnetic wave in the antenna, f is the frequency of the corresponding electromagnetic wave, c is the speed of light in the vacuum, and ε_e is the effective dielectric constant of the substrate.

For the proposed crack sensor fed by capacitive microstrip lines, the equivalent circuit according to the theory of transmission line [23] is shown in figure 3, when the patch antenna is excited by input electromagnetic waves at the feed point. The impedance of the circuit is composed of four parts: (1) the characteristic impedance of the rectangular patch antenna $Z(f)$, (2) the impedance of the bottom microstrip line without the overlapped part Z_b, (3) the impedance of the upper microstrip line without the overlapped part Z_u, and (4) the capacitive reactance X_C resulting from the capacitor of a pair of parallel overlapped microstrip lines. According to equation (1), the input impedance Z_{in1} of circuit in Box I can be calculated as

$$Z_{\text{in1}} = Z_b \frac{Z(f) + Z_b \tan \beta(l_b - \Delta l)}{Z_b + Z(f)\tan \beta(l_b - \Delta l)}, \tag{3}$$

where l_b and l_u is the length of the bottom microstrip line and the upper microstrip line respectively, and Δl is the overlapped length between them.

The circuit in Box I is treated as a cell, and it is in series with the capacitor. Therefore, the input impedance Z_{in2} of the circuit in Box II can be expressed as

$$Z_{\text{in2}} = Z_{\text{in1}} + \frac{f}{jC}, \tag{4}$$

where the second term in the right side of equation (4) represents the capacitive reactance X_C of the capacitor, and C represents the capacitance of the capacitor which can be described as

$$C = \frac{\varepsilon_{mr} S}{4\pi k d} = \frac{\varepsilon_{mr} w \Delta l}{4\pi k d}, \tag{5}$$

where ε_{mr} is the relative dielectric constant of the intermediate medium between the pair of overlapped microstrip lines, S is the overlapped area of the microstrip lines, w is the width of the bottom microstrip line and the upper microstrip line, d is the perpendicular distance between two microstrip lines, and k is the electrostatic constant.

Eventually, connected with equation (1), the input impedance Z_{in3} of the equivalent circuit of the crack sensor can be calculated as

$$Z_{\text{in3}} = Z_u \frac{Z_{\text{in2}} + Z_u \tan\beta(l_u - \Delta l)}{Z_u + Z_{\text{in2}} \tan\beta(l_u - \Delta l)}. \tag{6}$$

When a patch antenna operates at its resonant frequencies, its characteristic impedance can be described as [24]

$$Z(f_R) = \frac{60c^2}{W^2 {f_R}^2}, \tag{7}$$

where W represents the width of the antenna.

When the crack sensor is interrogated by a network analyzer via a coaxial line connected with the feed point, the impedance of crack sensor Z_{in3} is tailored to match the resistance of coaxial line R_t at the crack sensor's resonant frequency in order to minimize the reflected wave due to the medium discontinuity, which can be expressed as

$$Z_{\text{in3}} = R_t. \tag{8}$$

Substituting equations (1)–(7) into (8), the new equation can be derived as

$$Z_u \frac{\left(Z_b \frac{\frac{60c^2}{W^2 {f_R}^2} + j\left(\tan\frac{2\pi f_R}{c}\sqrt{\varepsilon_e}\right)(l_b - \Delta l) Z_b}{Z_b + j\left(\tan\frac{2\pi f_R}{c}\sqrt{\varepsilon_e}\right)(l_b - \Delta l)\frac{60c^2}{W^2 {f_R}^2}} + \frac{4\pi k d f_R}{\varepsilon_{mr} w \Delta l} \right) + j\left(\tan\frac{2\pi f_R}{c}\sqrt{\varepsilon_e}\right)(l_u - \Delta l) Z_u}{Z_2 + j\left(\tan\frac{2\pi f_R}{c}\sqrt{\varepsilon_e}\right)(l_u - \Delta l)\left(Z_b \frac{\frac{60c^2}{W^2 {f_R}^2} + j\left(\tan\frac{2\pi f_R}{c}\sqrt{\varepsilon_e}\right)(l_b - \Delta l) Z_b}{Z_b + j\left(\tan\frac{2\pi f_R}{c}\sqrt{\varepsilon_e}\right)(l_b - \Delta l)\frac{60c^2}{W^2 {f_R}^2}} + \frac{4\pi k d f_R}{\varepsilon_{mr} w \Delta l} \right)} = R_t. \tag{9}$$

In (9), c, k and R_t are constants, while W, w, l_b, l_u, d, ε_e, ε_{mr}, Z_b and Z_u are determined by the dimensions of the crack sensor, the material of substrate and the intermediate medium of the capacitor. Therefore, when a crack sensor is manufactured, the resonant frequencies of the crack sensor f_R are influenced only by the overlapped length Δl of the capacitor. We can write the resonant frequency of a fabricated crack sensor as a function of the overlapped length.

$$f_R = f_R(\Delta l), \tag{10}$$

Due to the detachable scheme of the transmission line, the proposed sensor can measure the displacement or crack width if each microstrip line is bonded with one side of a crack. The relative displacement of two microstrip lines will increase by the same amount as the crack propagates, which leads to the decrease of the overlapped length, and subsequently the resonant frequency of the crack sensor will shift. Crack width can be quantitatively determined once the relationship between resonant frequency of the crack sensor and crack width is established.

2.2. Design of crack sensors

2.2.1. Two prototypes of crack sensors. The cantilevered upper microstrip line of the proposed crack sensor should be firm enough to keep the gap distance stable. To meet this requirement, we propose two solutions for the cantilevered microstrip line.

(1) Prototype I: The capacitor gap filled with a dielectric slab.

As shown in figure 4(a), the parallel plate capacitor between microstrip lines is filled with a dielectric slab. The upper microstrip line is supported by the slab, which can move freely on the surface of the antenna substrate. The dielectric slab with the upper microstrip line is fixed with a connecting member. It is worth mentioning that the relative dielectric constant of the connecting member should be close to 1, which can be achieved with polymethacrylimide (PMI), which assures the induced electromagnetic field of the crack sensor will not be influenced by the connecting member.

The ground plane of the antenna and the connecting member are attached onto each side of a crack using adhesive glue. This detachable structure of the sensor will guarantee that no deformation of the substrate and no stress concentration issue is caused by a crack opening.

(2) Prototype II: The *L*-shaped cantilevered upper microstrip line.

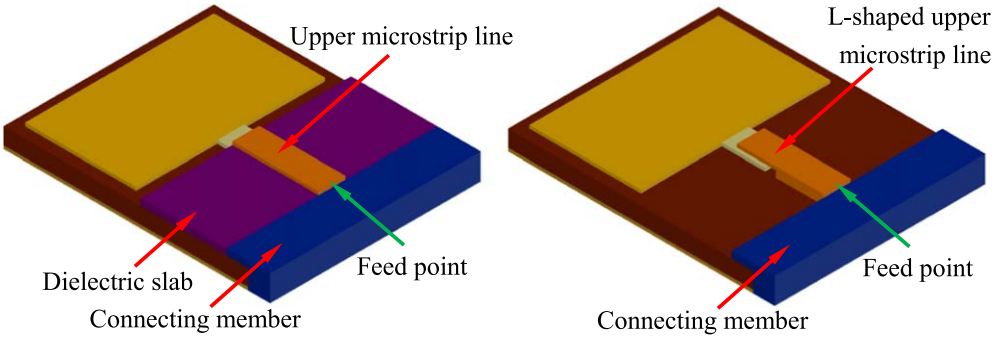

(a) The model with dielectric slab (b) The model with L-shaped upper microstrip line

Figure 4. Two prototypes of crack sensors.

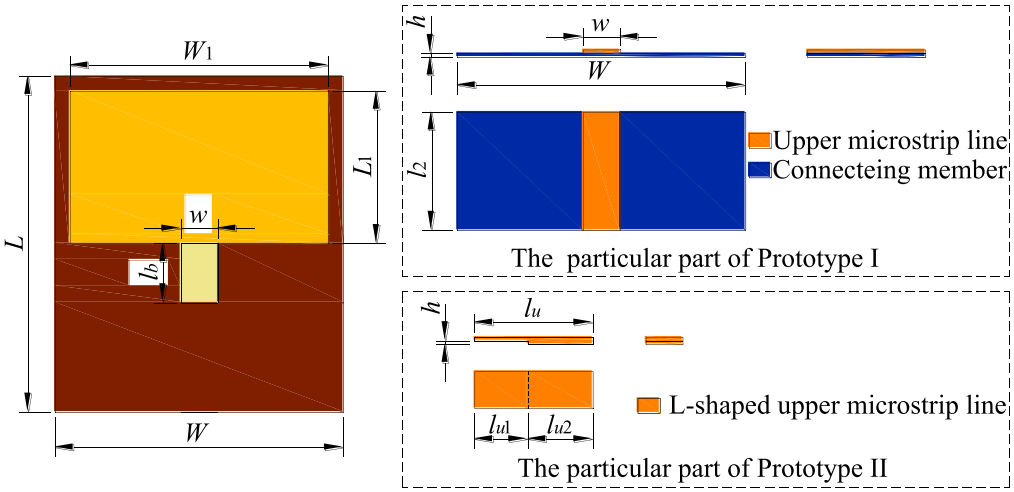

(a) Sharing integral part (b) Particular parts of two prototypes

Figure 5. Dimension of crack sensors.

Table 1. Optimal dimension of Prototype I (Unit: mm).

Parameters	L	W	L_1	W_1	l_b	w	l_u	h
Dimensions	45.4	39.0	20.6	35.0	8.0	5.0	16.0	0.5

As shown in figure 4(b), the cantilevered upper microstrip line is a *L*-shaped copper beam. Its cantilever beam overlaps with the bottom microstrip line forming a capacitor filled with air. Likewise, the connecting member connects to the *L*-shaped upper microstrip line, and the integral part is attached to one side of a crack.

2.2.2. Dimension design of crack sensors. A half-wavelength rectangular patch antenna has a dielectric substrate sandwiched between a radiation patch and a ground plane; thus, its initial resonant frequency can be calculated as [25]

$$f_{R0} = \frac{c}{2(L_1 + 2\Delta L_1)\sqrt{\varepsilon_e}}, \tag{11}$$

where L_1 is the length of the top radiation patch, ΔL_1 is the additional electrical length compensating the fringing effects due to the substrate thickness, and ε_e is the effective dielectric constant of the substrate, depending on the dimension of the antenna and relative dielectric constant of substrate ε_r.

Rogers RT/duroid 5880 is selected as the sandwiched substrate with a relative dielectric constant equal to 2.20. The thickness of the substrate is 0.5 mm, the standard size of this off-the-shelf item. The rectangular patch antenna is designed to operate approximately at the fundamental resonant frequency of 5 GHz for both prototypes. According to equation (11), the length of the radiation patch is given as 20.6 mm. The width of the radiation patch is 35 mm, as

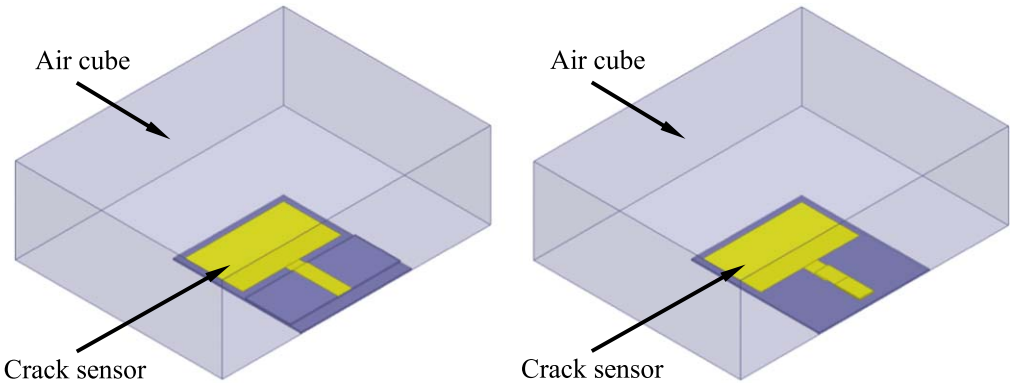

(a) Prototype I model (b) Prototype II model

Figure 6. The finite element models of crack sensors.

recommended by [26]:

$$W_1 = \frac{c}{2f_{R0}}\sqrt{\frac{\varepsilon_r + 1}{2}}. \tag{12}$$

The substrate and the ground plane have a dimension of 45.4 mm × 39 mm. For the crack sensor of Prototype I, the dielectric slab is the same material and thickness as the substrate, so the perpendicular distance between bottom microstrip line and upper microstrip line is determined as 0.5 mm. For consistency, we choose the gap distance of the capacitor as 0.5 mm for the other prototype.

To match the characteristic impedance of the crack sensor with the load of the connected coaxial cable as closely as possible, the dimensions of the bottom and upper microstrip lines should be optimized. The finite element software HFSS is used to simulate the crack sensors with different sizes of microstrip lines. The dimension parameters of two prototype sensors are shown in figure 5 and the corresponding dimensions are listed in tables 1 and 2.

3. Modeling and simulation of crack sensors

The finite element models of the two optimal crack sensors with capacitive microstrip lines are established in HFSS and shown in figure 6. The material of substrate and dielectric slab are selected as Rogers RT/duroid 5880, and the selected material of the *L*-shaped upper microstrip line is copper. The boundaries of the radiation patch, the ground plane, the bottom microstrip line, and the upper microstrip line are set as perfect *E*, which means their surfaces are perfectly perpendicular to the electric field. The bonding between the radiation patch, the ground plane and the bottom microstrip line are all assumed to be ideal with the substrate. The crack sensor is placed inside an air cube. The bottom surface of the crack sensors is in line with the bottom surface of the air cube, and the edge of the substrate is against the front surface of the cube. For the remaining surfaces and edges of the crack sensor, the distance between the sensor and the air cube in the same orientation is set as a quarter wavelength corresponding to the fundamental resonant frequency of the patch antenna. For the radiation boundary of the air cube, only radiating is assigned. The electromagnetic waves can be absorbed at the boundary of the air cube, meaning the boundary is extended to infinity.

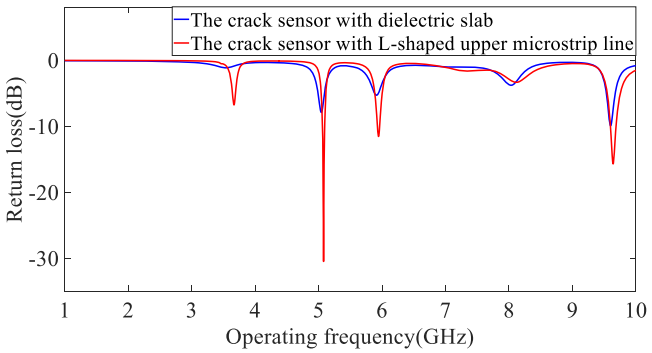

Figure 7. The return loss curves of two crack sensors with the same overlapped length.

3.1. Mode analysis of crack sensors

For numerical simulation, the initial overlapped lengths of both prototype sensors are set at 4 mm. A frequency domain solver is used to calculate the return loss curves within a frequency range from 1 to 10 GHz. The return loss S_{11} is defined as [27]

$$S_{11} = 10\lg\left|\frac{R_t - Z_{\text{in3}}^*}{R_t + Z_{\text{in3}}}\right|, \tag{13}$$

where Z_{in3}^* is conjugate with the input impedance of the crack sensor Z_{in3}, which varies with the operating frequency. When the crack sensor operates at its resonant frequencies, the impedance of the crack sensor and the impedance of the load match best. The crack sensor has multiple resonant modes. For each resonant mode, the return loss curve has its local minimum around the resonant frequencies, which can be described as

$$S_{11}(f_R) = \min[S_{11}(f)], f_R - \delta < f < f_R + \delta. \tag{14}$$

Table 2. Optimal dimension of Prototype II (Unit: mm).

Parameters	L	W	L_1	W_1	l_b	w	l_{u1}	l_{u2}	h
Dimensions	45.4	39.0	20.6	35.0	8.0	5.0	7.2	8.8	0.5

Table 3. The resonant frequencies and return loss of two crack sensors.

	Prototype I		Prototype II	
Order	Resonant frequency (GHz)	Return loss (dB)	Resonant frequency (GHz)	Return loss (dB)
1	3.5380	−1.13	3.6668	−6.74
2	5.0428	−7.89	5.0783	−30.47
3	5.9125	−5.29	5.9450	−11.53
4	8.0332	−3.78	8.1132	−3.34
5	9.6021	−9.91	9.6414	−15.68

The return loss curves of two prototype crack sensors are plotted in figure 7, and the resonant frequencies and corresponding return loss are listed in table 3, all of which were obtained from numerical simulation. Clearly, both crack sensors have several resonant frequencies within the featured frequency range. The corresponding resonant frequencies of the two crack sensors are close. This indicates the form of the upper microstrip line, either with a dielectric slab or a cantilevered copper beam, has limited influence on the resonant modes. Notably, the return loss of the Prototype II crack sensor has a smaller band width and a better noise-to-signal ratio at resonant frequencies than that of Prototype I. This proves that the sensor with the *L*-shaped upper microstrip line has better impedance matching than the sensor with the dielectric slab.

Taking the Prototype II crack sensor as an example, it has five resonant modes and corresponding resonant frequencies in a range from 1 to 10 GHz. The distribution patterns of the induced current on the radiation patch for each mode are illustrated in figure 8.

When the dimensions of the radiation patch are invariable, the induced current effect on radiation is solely dependent on time, which can be expressed as

$$i = \frac{dQ}{dt}, \tag{15}$$

where i is the induced current, and Q represents the quantity of electric charge. For the capacitor in the load of the patch antenna, the quantity of electric charge is relevant to the capacitance described by the following formula

$$Q = CU, \tag{16}$$

where U is the voltage between the two parallel plates of the capacitor. Substituting equations (16) and (5) into equation (15), the relationship between the induced current and the overlapped length of the capacitor can be derived.

$$i = \frac{\varepsilon_{mr} w \Delta l}{4\pi k d} \frac{\partial U}{\partial t}. \tag{17}$$

For resonant modes, the voltage of the capacitor harmonically oscillates with respect to time, which also applies to the current. According to equation (17), the amplitude of the induced current in the capacitive microstrip line will linearly vary with the overlapped length when the crack opens, further influencing the amplitude of the induced current in the radiation patch. Any change to the crack sensor's induced current will lead to a shift in resonant frequency [28].

For the first-order mode, the induced current comes from the bottom microstrip line and diffuses from the intersection of the radiation patch and the bottom microstrip line to the other three sides of the radiation patch. When the overlapped length of the pair of microstrip lines alters, the amplitude of induced current in the microstrip lines and radiation patch will vary.

The fundamental resonant frequency of the one-piece rectangular patch antenna was initially designed at around 5 GHz. Now this mode has become the second-order mode of the integral crack sensor because the capacitor in the transmission lines introduced a lower-order resonant mode with the current emitted from the capacitor. The induced current of the radiation patch flows along its longitudinal direction, and it is neutralized near the intersection area by the induced current coming from the bottom microstrip line because of their opposite directions. Basically, the change of the induced current amplitude has nothing to do with the overlapped length near the intersection area.

In the initial phase of the third-order mode, the induced current diffuses from the middle to both sides of the radiation patch and flows into the bottom microstrip line at a higher level, superimposed to the current emitted from the microstrip line. The superimposed current still depends on the shifting of the overlapped length. Because the Prototype II crack sensor has a low return loss at this mode, its resonant frequency is recommended for crack width sensing.

At the fourth and fifth-order modes, the induced current has multiple numbers of quarter waves in both directions. The coupled mechanism of the patch and the capacitor due to the complicated distribution pattern of the induced current cannot be explained and understood intuitively. It is worthy of experimental investigation in the future for possible adoption of the higher-order parameters as a sensing feature.

In conclusion, based on the extracted features of the proposed multi-mode sensors, the third-order resonant frequency of Prototype I and the first-order resonant frequency of Prototype II were chosen to monitor crack width.

3.2. Performance simulation of the crack sensor

3.2.1. The simulation of Prototype I. For the Prototype I crack sensor, the initial state of the crack sensor is two microstrip lines that fully overlap the length of the capacitor, which is equal to an 8 mm length of the bottom microstrip

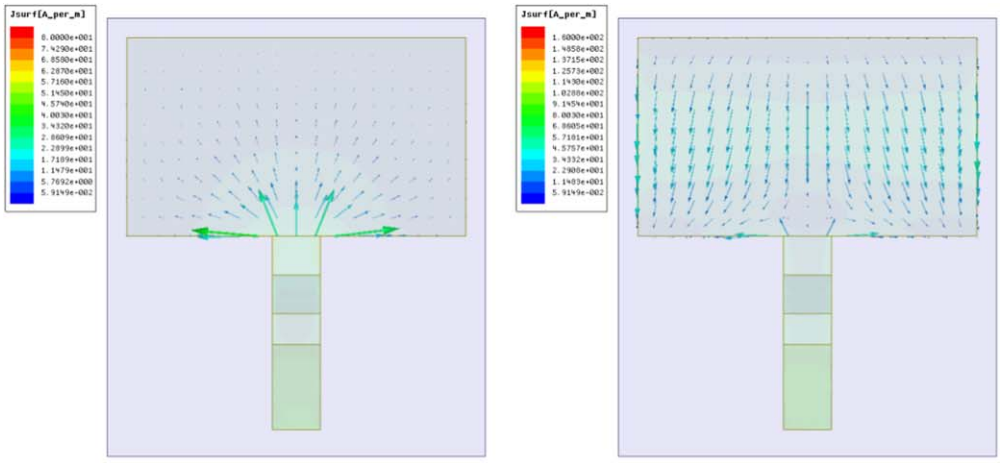

(a) First-order mode (b) Second-order mode

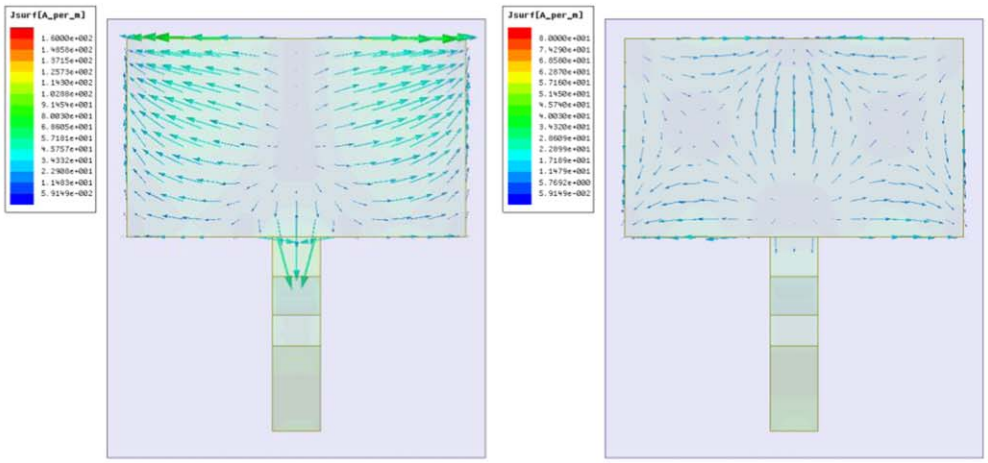

(c) Third-order mode (d) Fourth-order mode

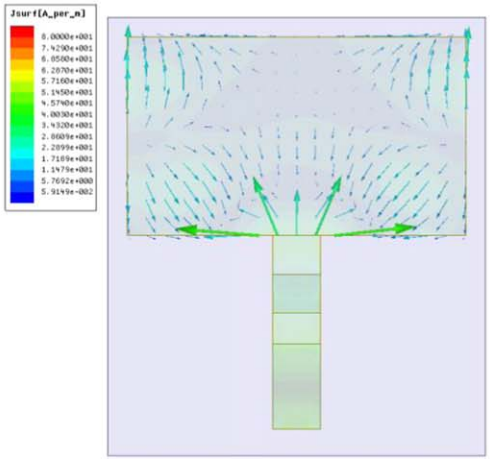

(e) Fifth-order mode

Figure 8. Distribution of induced current of crack sensors at different modes.

line. The overlapped length of the capacitor can move from 8 to 2 mm to simulate a crack propagation from 0 to 6 mm correspondingly. In the simulation, crack propagation is realized by applying a relative displacement between the bottom and upper microstrip lines at an incremental step of 0.1 mm. The return loss curve around the resonant frequency

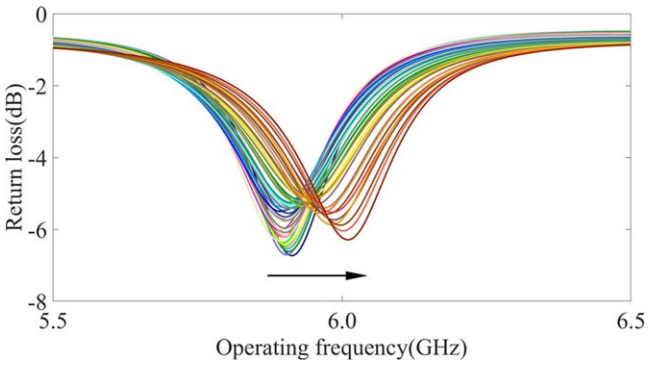

Figure 9. The return loss curves of the Prototype I crack sensor.

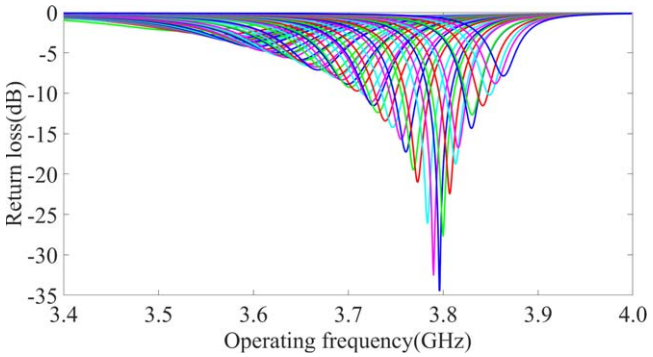

Figure 12. The return loss curves of the Prototype II crack sensor.

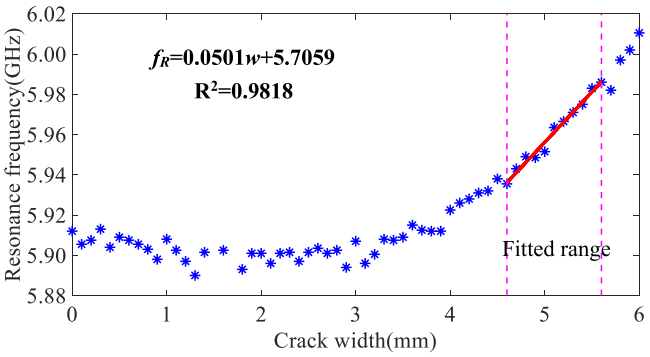

Figure 10. A scatter diagram and fitted line of the crack width-resonant frequency of the Prototype I crack sensor in the third-order mode.

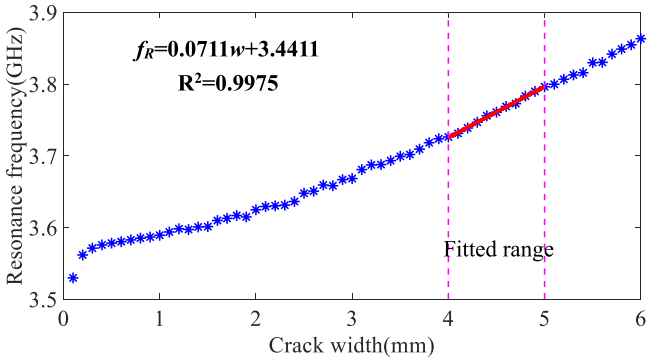

Figure 13. Scatter diagram and fitted line of crack width-resonant frequency of the Prototype II crack sensor.

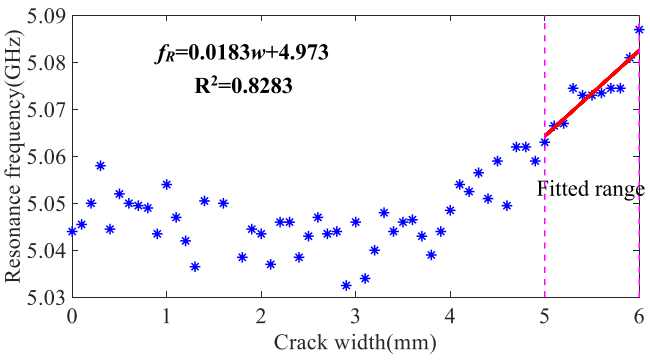

Figure 11. The scatter diagram and fitted line of crack width-resonant frequency of Prototype I crack sensor at second-order mode.

of the third-order mode is acquired at each crack width level, as shown in figure 9.

The third-order resonant frequency of the crack sensor is extracted from the return loss curve at each crack width level. The scatter diagram of resonant frequencies and the crack width is plotted in figure 10. For a crack width from 0 to 4 mm, no clear relationship exists between the resonant frequency and crack width, while the resonant frequency varies approximately linearly with the crack width between 4 mm and 6 mm.

For structures, a wider crack will accelerate the carbonation of concrete and the corrosion of the steel bars inside. So, the crack width is usually limited to a sub-millimeter level in building codes and standards [29–31]. Therefore, the effective measuring range is assigned within 1 mm. Based on the simulation result, the overlapped length between 3.4 and 2.4 mm are selected for sensing the width, where the correlation coefficient of the fitted line is closest to 1. The slope of the fitted line representing the sensitivity coefficient of the crack sensor is 0.0501 GHz mm^{-1}, with the resonant frequency of the crack sensor shifting 0.0501 GHz per millimeter. The orientation of crack is perpendicular to the longitudinal direction of crack sensor in our research. For other cases, the sensitivity coefficient needs to be adjusted by multiplying the cosine of the angle between the normal direction of crack and the longitudinal direction of sensor.

To verify the mode analysis, the second-order resonant frequency of Prototype I is extracted for each width increment, as plotted in figure 11. Obviously, the dataset between the frequency and the width are scattered more severely than that of the third-order mode. The potential segment utilized for sensing is only with the highest correlation coefficient of 0.8283, indicating that it is not the optimal choice for the extracted feature quantifying crack width.

3.2.2. The simulation of prototype II. For the crack sensor with the *L*-shaped upper microstrip line, the maximum overlapped length of the bottom microstrip line and the upper microstrip line is 7.2 mm, which is the length of the cantilever copper beam of the upper line. The range of crack

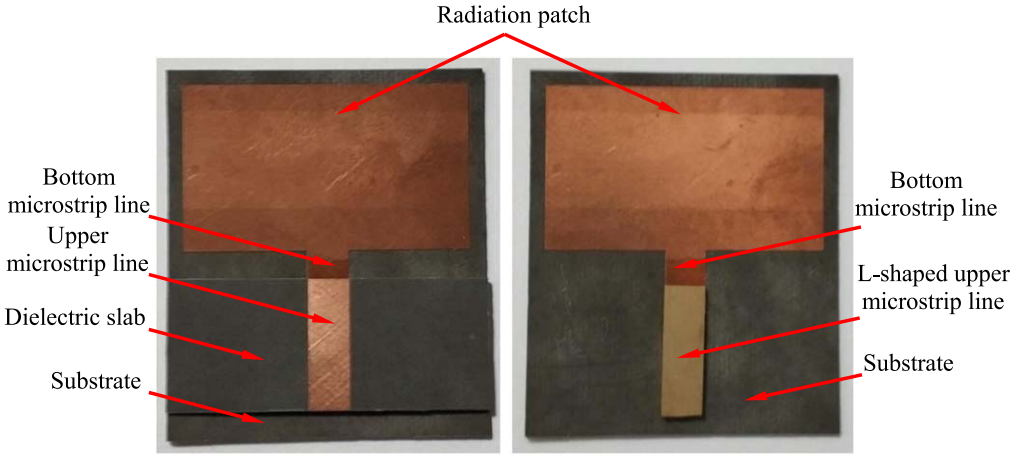

Figure 14. The manufactured crack sensors.

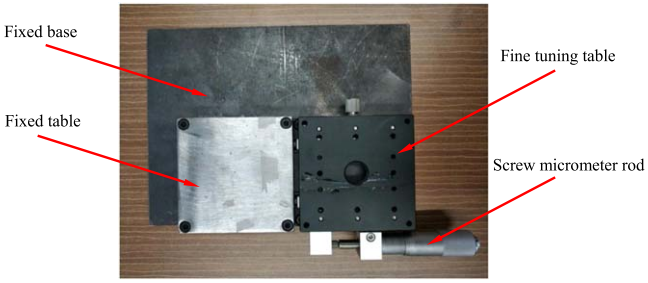

Figure 15. Simulator for crack propagation.

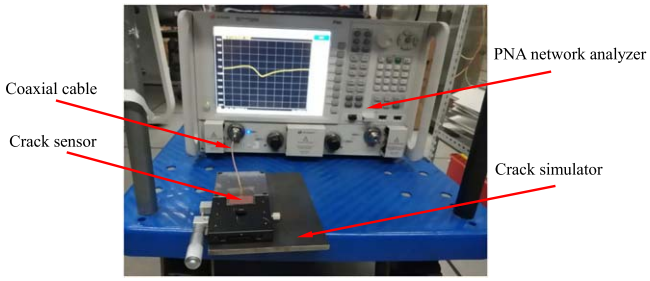

Figure 16. The experimental setup.

width is assigned from 0 to 6 mm, which means the overlapped length decreases from 7.2 to 1.2 mm to avoid letting the overlapped length become too small. The return loss curves are obtained numerically for each width step, and the segment around the first-order resonant frequency is shown in figure 12.

Then, we plot the first-order resonant frequency of Prototype II against the crack width in figure 13. Compared with figure 10, the first-order resonant frequency of the sensor increases monotonically with the crack in a more reliable manner. Similarly, the appropriate segment for width measurement were identified with the overlapped length from 3.2 to 2.2 mm. The sensitivity coefficient of Prototype II is 0.0711 GHz mm^{-1}.

4. Experiment of crack sensor

Rogers RT/duroid 5880 was selected as the middle substrate of the rectangular patch antenna and the bottom microstrip line. This sharing integral part for both prototypes and the dielectric slab with the upper microstrip line described in table 1 were tailored by a professional institute. And the cantilevered copper beam of Prototype II was manufactured from a copper block. The two different sensor prototypes of sensors with capacitive microstrip lines are shown in figure 14.

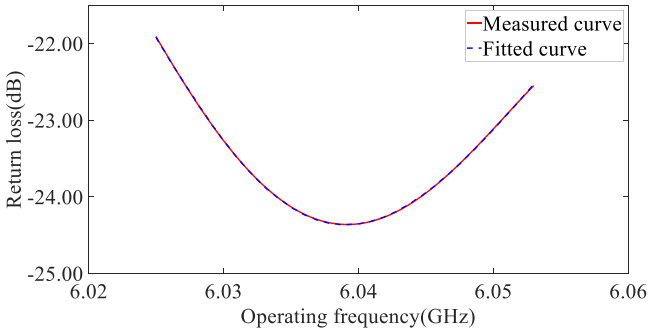

Figure 17. Comparison of measured curve and fitted curve.

4.1. Instrumentation setup

A device able to simulate the crack propagation is shown in figure 15. A fixed table and a fine tuning table are mounted on one base plate, and the fine tuning table can move toward and against the fixed table, which is controlled by a screw micrometer rod with a minimum precision of 0.01 mm.

The sharing integral part was attached to the fixed table by glue, and the dielectric slab or the *L*-shaped upper transmission line was bonded with the tuning table by adhesive tape, acting as the connecting member. The upper microstrip line was connected to a Keysight N5227A PNA Network Analyzer (Keysight Technologies, Santa Rosa, CA, USA) using a coaxial cable shown in figure 16. The PNA feeds the patch antenna with the electromagnetic wave within a certain

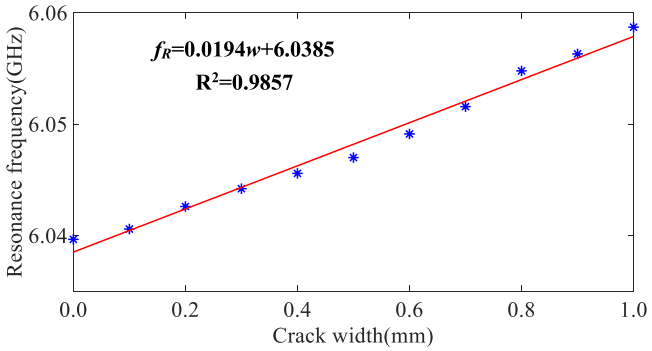

Figure 18. Resonant frequency with respect to crack width of Prototype I.

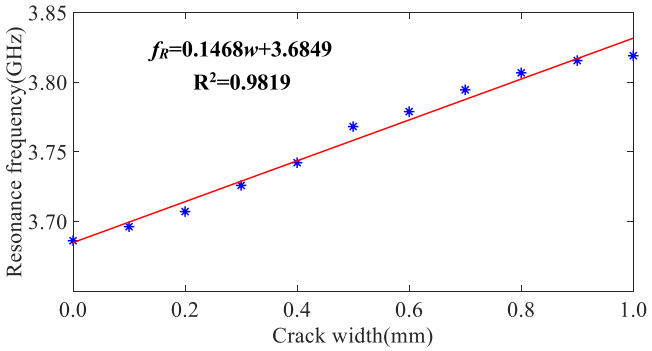

Figure 19. Resonant frequency with respect to the crack width of Prototype II.

frequency range around the resonant frequency determined by simulation through the microstrip transmission line and receives the reflected wave by the antenna. In this way, the return loss curve of the crack sensor can be obtained.

The crack propagation experiments were carried out for each prototype sensor.

(1) Prototype I crack sensor: the crack width was simulated from 0 to 1 mm, setting the crack sensor with the initial state of the overlapped length equal to 3.4 mm. The crack was opened wider from 0 to 1 mm at a step of 0.1 mm using a screw micrometer rod. For each step, the return loss curve of the crack sensor was measured using the PNA five times by sweeping the interrogation frequency from 5.75 to 6.25 GHz with a frequency step of 100 kHz.
(2) Prototype II crack sensor: the initial state of the crack sensor with the *L*-shaped upper microstrip line was set at an overlapped length of 3.2 mm. The crack sensor was tested at different width increment resolutions. The crack width was increased from 0 to 1 mm at a width resolution of 0.1 mm, with the overlapped length decreased from 3.2 to 2.2 mm. At a finer resolution of 0.01 mm, the crack sensor was tested with the opening of crack from 0 to 0.1 m. For each step, the return loss curve of the crack sensor was extracted from the PNA. The frequency sweepings are all from 3.5 to 4.0 GHz. A total of 5001 frequency points were obtained.

4.2. Results and discussion

To reduce experimental error, the return loss curves of the crack sensor were tested five times at each crack width level. The quartic polynomial curve was utilized to fit the return loss curve around the area of desired resonant frequencies. The resonant frequency at the local minimum was extracted for each curve. The comparison of the measured curve and fitted curve around the desired resonant frequencies is shown in figure 17. Five identified resonance frequencies of the crack sensor were averaged at each crack width level. The Dixon criterion [32] was used to eliminate the outlier from this data set judged by a given confidence level of 95%.

4.2.1. Result analysis of prototype I crack sensor. Before the crack propagation experiment, the resonant frequency of the Prototype I sensor predicted by the numerical simulation was first validated by a PNA network analyzer sweeping in the state of the overlapped length equal to 3.4 mm. Its initial resonant frequency of the third mode was 6.0393 GHz, slightly differing from the simulated frequency of 5.9355 GHz with a relative error of 1.72%.

As the crack gradually opened, the third-order resonant frequency of the crack sensor was retrieved at each width level and linearly fitted with respect to the crack width, as shown in figure 18. The correlation coefficient of the fitted line is 0.9857, indicating that the third-order resonant frequency of Prototype I has an excellent linear relationship with the crack width.

The measured sensitivity coefficient of the third-order resonant frequency to width was 0.0194 GHz mm^{-1}, which deviated significantly from the simulated sensitivity of 0.0501 GHz mm^{-1}. This big difference is probably due to the following reasons.

(1) There was practically a gap between the bottom microstrip line and dielectric slab, which was filled with air. This situation did not coincide with the simulation on the parallel gap filled only with RT5880 between the bottom and upper microstrip lines, causing a difference between the simulation and experiment.
(2) During the experiment, the symmetric axis of microstrip lines may not be aligned with each other, making the overlapped area different from simulations. Further, there is nonlinear relationship between the capacitance and the overlapped length of the capacitor when two microstrip lines are not parallel to each other, magnifying the difference between simulations and experiments.
(3) In the experiment, the end of the upper microstrip line was soldered with a coaxial cable connecting the PNA. The position, size and shape of the soldering point influenced the impedance of the transmission line and subsequently altered the resonant frequencies of the crack sensor.
(4) The electromagnetic interference coming from the surroundings' reflection [33] and the environmental

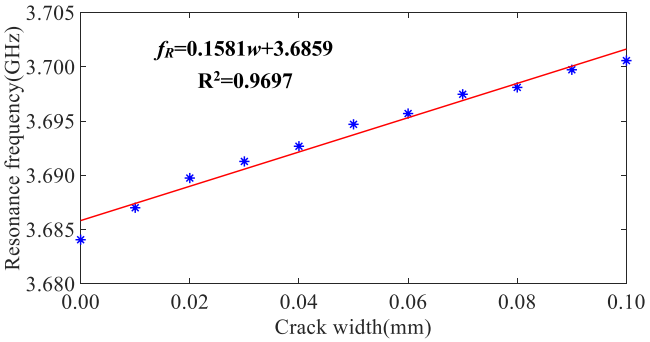

Figure 20. Resonant frequency with respect to crack width of Prototype II (Step:0.01 mm).

temperature [34] will also have an effect on the resonant frequencies of crack sensors in experiments.

4.2.2. Result analysis of prototype II crack sensor. Similarly, we verified the simulated resonant frequency of the Prototype II sensor at the initial state through sweeping wave excitation by a PNA. The measured resonant frequency at the first-order mode was 3.6862 GHz with a slight difference in the simulation result of 3.726 5 GHz (i.e., a relative error of 1.08%).

The crack opening experiments were conducted at two different width resolutions. For a coarser resolution of 0.1 mm, the first-order resonant frequency of Prototype II was obtained and fitted with respect to the crack width, as presented in figure 19.

The correlation coefficient of the fitted line between the frequency and the crack width is 0.9819. The measured sensitivity coefficient of Prototype II is 0.0711 GHz mm^{-1}, while the simulated sensitivity is 0.1468 GHz mm^{-1}. The possible reasons for this substantial difference are the rough bottom surface of the *L*-shaped upper microstrip line, misalignment between the pair of microstrip lines, variable shapes of the soldering point between the transmission line and the coaxial cable, and environmental noises.

The crack opening was repeated at a finer resolution of 0.01 mm from 0.0 to 0.1 mm. Likewise, the first-order resonant frequency of Prototype II which varied with the width is plotted in figure 20 with a linear fitting. The correlation coefficient is 0.9697, and the sensitivity coefficient of the crack sensor is 0.1581 GHz mm^{-1}, exhibiting a bit difference from the former test. This demonstrates the disturbances are prone to be magnified due to the tiny resonant frequency shift of the crack sensor under the fine step. Apparently, Prototype II can achieve better resolution of 0.01 mm, and has more reliable performance than Prototype I.

5. Conclusions

This paper demonstrated a novel crack sensor based on a patch antenna fed by capacitive microstrip lines, which are capable of sensing crack widths on a structure. Simplified by the model of transmission line for a patch antenna, a linear relationship exists between the resonant frequency of crack sensors and the overlapped length between the bottom and upper microstrip lines of the crack sensors. Two crack sensor prototypes were designed and fabricated using a dielectric slab and an *L*-shaped upper microstrip line, respectively. The experiment results validated that the extracted resonant frequencies of crack sensors depend on crack width as a linear function, and a crack sensor with an *L*-shaped upper microstrip line can detect a crack width within a hundredth of a millimeter. The sensitivity coefficients of the crack sensors obtained from experiments differed significantly from the value of numerical simulations due to fabrication errors and environmental interference.

In the future, we will explore chipped crack sensors via wireless interrogation to cancel the effects caused by the soldering point of the coaxial cable. When using radio frequency identification, the novel method to extract the features of antenna sensors will be adopted, such as transient responses from in-phase quadrature signal [35], overcoming the challenges of low sensitivity and robustness along with the power-based features. Furthermore, in order to reduce the dimensions of sensors, the attention on miniaturization will be paid, which can be realized by redesigning the shape of radiation patch [36, 37].

Acknowledgments

This study was supported by the Key Program of Intergovernmental International Scientific and Technological Innovation Cooperation (No. 2016YFE0127600), the Key Laboratory of Performance Evolution and Control for Engineering Structures (Tongji University), the Ministry of Education (No. 2018KF-4), and the Fundamental Research Funds for the Central Universities.

ORCID iDs

Kangqian Xu https://orcid.org/0000-0002-6198-3982
Liyu Xie https://orcid.org/0000-0001-5777-0645

References

[1] Sohn H 2004 A review of structural health monitoring literature: 1996–2001 *Data Acquisition* LA-13976-MS Los Alamos: Los Alamos National Laboratory
[2] Al-Sulaimani G J *et al* 1990 Influence of corrosion and cracking on bond behavior and strength of reinforced concrete members *Aci Struct. J.* **87** 220–31
[3] Kujawski D and Ellyin F 1984 A fatigue crack propagation model *Eng. Fract. Mech.* **20** 695–704
[4] Roylance D 2001 *Introduction to Fracture Mechanics* vol 1 (Cambridge: Massachusetts Institute of Technology) (https://doi.org/10.13140/RG.2.1.1444.2408)
[5] Mahmoud A M *et al* 2010 Non-destructive ultrasonic evaluation of CFRP–concrete specimens subjected to accelerated aging conditions *Ndt & E Int.* **43** 635–41

[6] Gu X, Chen Z and Ansari F 2000 Embedded fiber optic crack sensor for reinforced concrete structures *Aci Struct. J.* **97** 468–76
[7] Butler J C *et al* 2002 Wireless, passive, resonant-circuit, inductively coupled, inductive strain sensor *Sensors Actuators* A **102** 61–6
[8] Zhang J *et al* 2017 A review of passive RFID tag antenna-based sensors and systems for structural health monitoring applications *Sensors* **17** 265
[9] Huang H 2014 Antenna sensors in passive wireless sensing systems *Handbook of Antenna Technologies* (Singapore: Springer) pp 1–34
[10] Daliri A *et al* 2012 Utilising microstrip patch antenna strain sensors for structural health monitoring *J. Intell. Mater. Syst. Struct.* **23** 169–82
[11] Yi X *et al* 2011 Passive wireless smart-skin sensor using RFID-based folded patch antennas *Int. J. Smart Nano Mater.* **2** 22–38
[12] Yi X *et al* 2013 Passive wireless antenna sensor for strain and crack sensing—electromagnetic modeling, simulation, and testing *Smart Mater. Struct.* **22** 85009
[13] Deivasigamani A *et al* 2013 A review of passive wireless sensors for structural health monitoring *Modern Appl. Sci.* **7** 57–76
[14] Li S *et al* 2006 Radio frequency identification technology: applications, technical challenges and strategies *Sensor Rev.* **26** 193–202
[15] Mohammad I and Huang H 2010 Monitoring fatigue crack growth and opening using antenna sensors *Smart Mater. Struct.* **19** 55023
[16] Hasani M *et al* 2015 A novel enhanced-performance flexible RFID-enabled embroidered wireless integrated module for sensing applications *IEEE Trans. Compon. Packag. Manuf. Technol.* **5** 1244–52
[17] Thai T T *et al* 2011 Design of a highly sensitive wireless passive RF strain transducer *Microwave Symp. Digest(MTT), 2011 IEEE MTT-S Int. (Daejeon)* (https://doi.org/10.1109/MWSYM.2011.5972980)
[18] Thai T T *et al* 2013 Novel design of a highly sensitive RF strain transducer for passive and remote sensing in two dimensions *IEEE Trans. Microw. Theory Tech.* **61** 1385–96
[19] Tata U *et al* 2008 Exploiting a patch antenna for strain measurements *Meas. Sci. Technol.* **20** 15201
[20] Cho C *et al* 2016 Passive wireless frequency doubling antenna sensor for strain and crack sensing *IEEE Sensors J.* **16** 5725–33
[21] Caizzone S, Digiampaolo E and Marrocco G 2014 Wireless crack monitoring by stationary phase measurements from coupled RFID tags *IEEE Trans. Antennas Propag.* **62** 6412–9
[22] Caizzone S and Digiampaolo E 2015 Wireless passive RFID crack width sensor for structural health monitoring *IEEE Sensors J.* **15** 6767–74
[23] Pozar D M 2009 *Microwave Engineering* (Chichester: Wiley)
[24] Bahl I J and Bhartia P 1980 *Microstrip Antennas* (Deldham, MA: Artech)
[25] Stutzman W L and Thiele G A 2013 *Antenna Theory and Design* (Chichester: Wiley) (https://doi.org/10.1049/ep.1982.0113)
[26] Constantine A B 2005 *Antenna Theory: Analysis and Design* (Chichester: Wiley)
[27] Kurokawa K 1965 Power waves and the scattering matrix *IEEE Trans. Microw. Theory Tech.* **13** 194–202
[28] Mosig J and Gardiol F 1979 The near field of an open microstrip structure *IEEE Antennas & Propagation Society Int. Symp. (Washington)* (https://doi.org/10.1109/APS.1979.11481962)
[29] 2014 Building code requirements for structural concrete (ACI 318-14) and commentary. American Concrete Institute
[30] 2004 2004 Eurocode 2: Design of concrete structures Part 1-1–General rules and rules for buildings. London: British Standards Institution
[31] 2010 Code for design of concrete structures (GB 50010-2010). Ministry of Housing and Urban-Rural Development of the People's Republic of China
[32] Verma S P and Ruiz A Q 2006 Critical values for six dixon tests for outliers in normal samples up to sizes 100, and applications in science and engineering *Rev. Mex. de Cienc. Geológicas* **23** 133–61
[33] Xu X and Huang H 2012 Battery-less wireless interrogation of microstrip patch antenna for strain sensing *Smart Mater. Struct.* **21** 125007
[34] Tchafa F M and Huang H 2018 Microstrip patch antenna for simultaneous strain and temperature sensing *Smart Mater. Struct.* **27** 65019
[35] Zhao A, Tian G Y and Zhang J 2018 IQ signal based RFID sensors for defect detection and characterisation *Sensors Actuators* A **269** 14–21
[36] Zhao A, Zhang J and Tian G Y 2017 Miniaturization of UHF RFID tag antenna sensors for corrosion characterization *IEEE Sensors J.* **17** 7908–16
[37] Ng W *et al* 2019 Compact planar inverted-S antenna with embedded tuning arm for on-metal UHF RFID tag design *IEEE Trans. Antennas Propag.* **67** 4247–52